Ultrafast Structural Dynamics of the Photocleavage of Protein Hybrid Nanoparticles

Shyjumon Ibrahimkutty,[†] Jangbae Kim,[‡] Marco Cammarata,[§] Friederike Ewald,[§] Jungkweon Choi,[‡] Hyotcherl Ihee,[*,‡] and Anton Plech[†,¶,*]

[†]Institute for Synchrotron Radiation, Karlsruhe Institute of Technology, Postfach 3640, D-76021 Karlsruhe, EU, [‡]Center for Time-Resolved Diffraction, Department of Chemistry, Graduate School of Nanoscience & Technology (WCU), Yuseung-gu, Daejeon, 305-701, South Korea, and [§]ESRF, BP 220, 6, rue J. Horovitz, F-38043 Grenoble, EU. [¶] Center for Applied Photonics, University of Konstanz, Universitätsstrasse 10, D-78457 Konstanz, EU.

ABSTRACT Protein-coated gold nanoparticles in suspension are excited by intense laser pulses to mimic the light-induced effect on biomolecules that occur in photothermal laser therapy with nanoparticles as photosensitizer. Ultrafast X-ray scattering employed to access the nanoscale structural modifications of the protein—nanoparticle hybrid reveals that the protein shell is expelled as a whole without denaturation at a laser fluence that coincides with the bubble formation threshold. In this ultrafast heating mediated by the nanoparticles, time-resolved scattering data show that proteins are not denatured in terms of secondary structure even at much higher temperatures than the static thermal denaturation temperature, probably because time is too short for the proteins to unfold and the temperature stimulus has vanished before this motion sets in. Consequently the laser pulse length has a strong influence on whether the end result is the ligand detachment (for example drug delivery) or biomaterial degradation.

KEYWORDS: protein-nanoparticle hybrids · photo-cleavage · thermal denaturation · pulsed X-ray scattering · nanobubbles

Biological application of nanoparticles include the hybridization with proteins, or specifically with antibodies for *in-vitro* and *in-vivo* labeling of the corresponding tissue containing the antigenes. While nanoparticles may enhance the detection threshold for targeted tissues, they can also be used in a second step as local tools for tissue modification. It has been shown that laser-excited gold particles can enhance transfection through cell walls by transiently enhanced permeation of the cell walls.[1,2] A large number of studies have focused on the effect of laser-heated particles, in particular of gold for cell destruction.[3−5]

The thermal kinetics of laser-excited metal nanoparticles is already well understood, which includes a plasmonic excitation of the conduction electron gas, a subsequent thermalization and coupling to the lattice, and the generation of heat. The heat dissipates with time constants in the nanosecond range into the local surrounding and thus into the adjacent biological tissue. Optical methods such as fluorescence lifetime methods or UV circular dichroism that probe the change in the plasmon resonance of the particles, in particular in the case of gold or silver particles, usually give only indirect access to the thermal state on the nanoscale without directly probing the primary structural modifications. On the other hand structural methods, such as ultrafast electron scattering[6,7] and X-ray scattering have been successfully applied to study the photokinetics of small molecules,[8−11] tertiary and quaternary protein movement,[12] or the rich structural response in pure nanoparticle systems.[13−15]

Here we show that in the model hybrid system of gold nanoparticle—bovine serum albumin (BSA) it is possible to follow the photoinduced structural response of the protein layer at a well-defined temperature and time scale both on a mesoscopic scale and for structural motifs of the proteins. Figure 1 visualizes two candidate reactions from particle heating: protein denaturation and protein cleavage from the surface. These two pathways will differ critically in the final impact on the protein in a practical application.

The study is conducted as a two-color pump—probe experiment with a laser pulse as ultrafast heat source and a temporally synchronized X-ray pulse as structural probe. Because of the low scattering cross section and the dilution of the samples, multiple shots have to be accumulated on the X-ray detector for obtaining meaningful data. At the same time the experiment has to be designed as single-shot excitation due to the irreversible nature of the protein excitation. The synchrotron-based scattering allows for a 100 ps time resolution.

* Address correspondence to hyotcherl.ihee@kaist.ac.kr, anton.plech@kit.edu.

Received for review January 12, 2011 and accepted April 19, 2011.

Published online April 19, 2011
10.1021/nn200120e

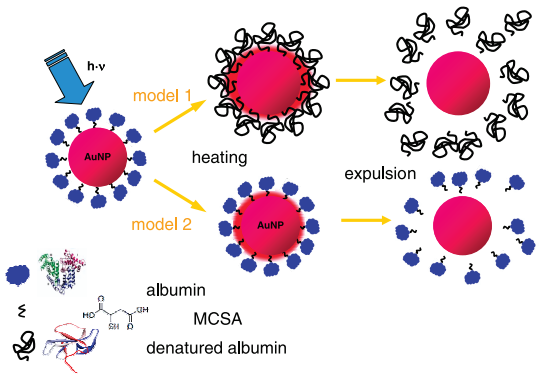

Figure 1. Schematic pathway for the photocleavage of protein-coated gold nanoparticles. The bovine serum albumin is coupled to the particles *via* a thiol linker (MCSA). After the photoexcitation the temperature increase outside the nanoparticles within 100 ps may cause a fast denaturation (model 1), which is eventually followed by expulsion at a fluence above the bubble formation threshold. Alternatively the protein may be expelled without a denaturation step (model 2).

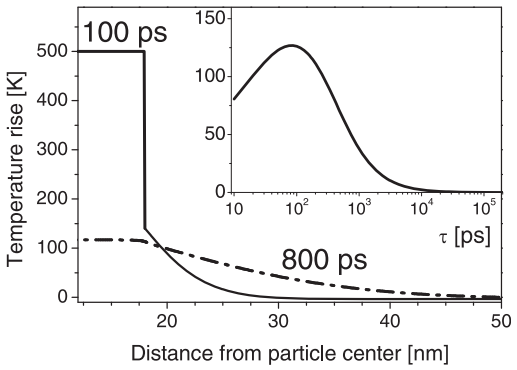

Figure 2. Calculated temperature profile around a femtosecond laser excited gold nanoparticle as a function of distance from the particle center at 100 ps (solid) and 800 ps (dotted). The initial temperature rise within the particle is taken as 500 K. The inset shows the temperature rise in the adjacent layer outside of the particle as a function of time delay after the laser excitation.

RESULTS AND DISCUSSION

Thermokinetics of the Excited Nanoparticles. The thermal kinetics of suspended nanoparticles following femtosecond laser excitation is quite well understood, both by optical spectroscopy[16−18] and pulsed X-ray scattering.[13,14] Heat dissipation can be understood down to the 10 nm scale by conventional macroscopic heat transfer, with one exception being that the interface resistance (Kapitza resistance) cannot be neglected. The interface resistance accounts for a finite probability of phonons crossing the particle−water interface due to the acoustic mismatch. The numerical approaches have shown to reproduce the heat dissipation fairly well, thereby allowing the quantification of the Kapitza resistance.[19]

One practical aspect of this kinetics is that the heat transfer from the particle to the surrounding matrix (water or protein in the present case) is delayed. There will always be a step in temperature across the interface, so that the temperature reached in the surrounding layer will be considerably lower than the nanoparticle lattice. Figure 2 shows an example of such a calculation for bare gold particles, where an initial temperature rise of 500 K in the particle is assumed. At a delay of 100 ps after laser excitation the particle temperature is still almost at maximum, while some heat has dissipated within the first 10 nm of the surrounding water. At 800 ps the particle has cooled down significantly, heating up a region of some 40 nm rather homogeneously. At even later times the heat dissipation into the bulk water takes place. The inset in Figure 2 shows the temperature history in the water layer in contact with the nanoparticle. It reaches a flat maximum at around 150 ps and then goes down to ambient values within the dissipation time of about 500 ps. The maximum temperature rise is characteristic for a given particle size. The maximum particle temperature, on the other hand, is given by the laser fluence. The fluence is indeed a good control parameter as the deposition of laser energy is faster than any of the structural relaxation processes, in particular the particle cooling. The temperature can be calibrated by a control experiment.[13] Thus we can relate directly the maximum adjacent water temperature to the laser fluence to a precision of about 20 %, which includes particle size dispersion, shot-to-shot fluence variations and the spatial variation of fluence across the X-ray focus.

Implicitly it was assumed that the heat transfer equations are not directly temperature dependent, such as through temperature dependent heat conductivity. This has shown to be true in a temperature interval of some hundred K.[13] However, one important nonlinearity is the explosive boiling of the water phase once the temperature surpassed the spinodal temperature for water. As consequence nanometric bubbles form symmetrically around the heated nanoparticles, which grow and collapse within a 1−2 ns time scale.[14,20]

In SAXS one will therefore observe large scattering changes once the bubble formation threshold is surpassed, which can be seen in Figure 3. For the bare particles below (92 J/m^2) the threshold fluence the difference invariant (excited minus non-excited) is almost zero except for a tiny negative signal within the first 100 ps after excitation, which reflects the transient heating and therefore slight density change of the surrounding water layer. At a fluence value far above (425 J/m^2) the threshold a large transient is observable. It reflects the appearance and collapse of vapor bubbles around the particles. After the collapse the invariant almost (except from a tiny offset) returns to the nonexcited value, indicating the reversibility of the process.

A completely different picture is revealed for BSA-coated nanoparticles. At the same low fluence there is

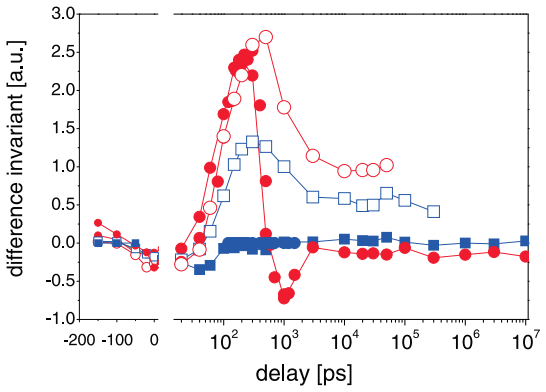

Figure 3. SAXS Porod invariant signal according to eq 2 of nanoparticles excited with a fluence for bare particles (filled symbols) and BSA-coated nanoparticles (open symbols) below (blue squares) and above (red circles) the bubble formation threshold as a function of time delay.

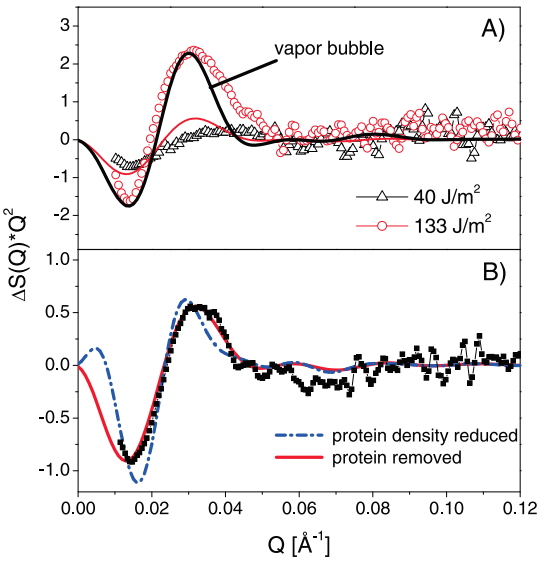

Figure 4. (A) Difference $\Delta S(Q) \times Q^2$ of SAXS intensities of 17 nm BSA-coated gold nanoparticles before and after laser excitation at different laser fluences of 40 J/m^2 (triangles) and 133 J/m^2 (circles) and 250 ps delay. The lines are the model for protein shell removal (red line) and formation of a bubble of 1.45 times the particle radius (bold black line). (B) The same for high laser fluence (>60 J/m^2) and averaged for time delays between 10 and 100 ns (dots). The lines are fits according to the model of a protein shell of reduced density (model 1, blue dash dotted line) and removed protein shell (model 2, full red line). The second model explains the experimental data better than the first model.

already a strong transient change of the invariant, followed by a persistent difference. Here the absorption cross section increases slightly due to the stabilization of the plasmonic resonance of the particles in a medium with higher dielectric constant. Therefore a fraction of the particles already surpass the bubble formation threshold and some bubble nuclei are formed. The persistent change already indicates that the particle−shell structure has been perturbed permanently. At the higher laser fluence fully developed bubbles occur, followed by a larger persistent change.

Protein Shell Expulsion. While the bubble formation is an effect of the uncoated nanoparticles as well as the protein-coated nanoparticles, the persistent change is solely seen for the hybridized system. The bubble signature can be seen in Figure 4A for a fluence of 133 J/m^2. It can be modeled by only a vapor bubble around the particle of 1.45 times the particle radius. The main difference to the protein removal (and thus density reduction) is the amplitude of the difference signal. At higher bubble sizes the signal will shift in position as well. At the lower fluence (40 J/m^2) a small modulation of the difference scattering is visible, which stems from a small density change due to heating. An analysis of the SAXS pattern at longer times (Figure 4B) after the transient evaporation process has decayed, shows an oscillatory structure, which is best explained by a complete expulsion of the BSA layer from the particle surface. A comparison is made for two different models of the modification of the BSA layer against the scattering difference. The first model assumes that BSA remains attached to the particles, but only its density is reduced while the thickness increases to mimic a transition from a folded protein to a random coil with extending strands of protein. In the second model the complete layer of BSA, having a density of 1.35 g/cm^3, is removed from the particle surface. Although the first model can reproduce in general the sign of the oscillations with an increase of the protein layer from 9 nm thickness to 17 nm and accordingly reducing the density, a much better fit is obtained by model 2. Values for the (hydrated) density of BSA in the range of 1.35 g/cm^3 have been reported,[21] which agree well with our density fit. This implies that during the photoexcitation the protein shell is completely removed from the particle surface and does not recombine during the observation interval (1 μs). The static SAXS measurements have revealed a density change of the adsorbed shell of only 19 % when adding BSA to the MCSA-coated particles. This slight discrepancy may, however, be due to a smaller density change with only BSA addition onto the MCSA terminated particles, while during the photodesorption the entire coating of BSA plus MCSA is expelled. The underlying breakage of the thiol bond during photoexcitation has been reported earlier.[22] By a comparison of the long time signal to the signal at 250 ps and 40 J/m^2 it seems that the protein layer was not totally removed as neither model 1 nor model 2 fully explain the modulation in Figure 4A.

In consequence all structure changes are finished within the bubble dynamics interval, whereafter no further changes occur. Indeed the shape of the difference scattering in Figure 4 is independent of the applied laser fluence, and only the amplitude of its signal changes for low fluence values and for long delays. Using this fact the signal amplitude can serve as a quantitative measure of efficiency of protein expulsion. We can obtain the transient temperature rise that

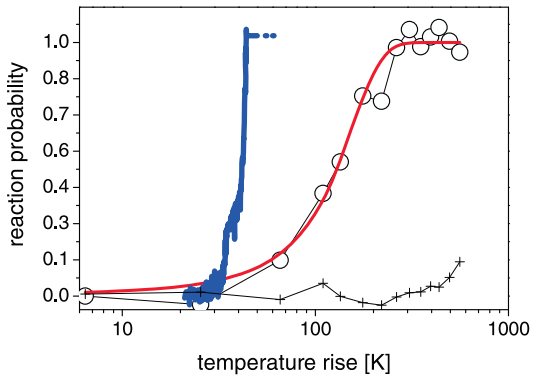

Figure 5. Reaction probability derived from the signal amplitude in Figure 4B of the excited BSA-coated particles as a function of maximum temperature rise in the liquid shell around the nanoparticles (open circles) as well as a control experiment without BSA (crosses). A fit with a rate process function is shown as a red line. The bold blue line displays an analogue probability from the SAXS signal change during thermal denaturation.

the protein must have suffered within the first few hundreds of picoseconds, by using the calibration of temperature *versus* fluence.[14]

In Figure 5 the reaction probability (normalized signal amplitude) from Figure 4 has been plotted against the maximum temperature rise adjacent to the nanoparticles. The high temperature limit is used as a scaling factor to define a reaction (=desorption) probability from 0 to 1. A rate equation with a sigmoidal distribution describes the behavior well (see Supporting Information). The solid line shows a fit to the experimental data assuming this sigmoidal reaction probability. Following this result the protein layer is only expelled at a temperature rise of around 100−160 K in the water phase (50% value at 129 K), which agrees well with the bubble formation threshold, which would be located at 120 K for bare particles. Secondly and more interestingly the ΔS curves fall on top of each other when they are scaled with the inverse of the reaction probability. This means that the protein shell density is not affected at all in its structure below a temperature rise of some 70 K or even up to the threshold. Also shown in Figure 5 is the SAXS signal change for static heating of BSA-coated particles as a function of temperature, where the reaction probability is defined as the change of the SAXS signal. In strong contrast to the laser irradiated case, a strong change in SAXS signal is observed already for a temperature rise of 42 K. This rise amounts to an absolute temperature of the suspension of 65 °C. Such a curve of the change of SAXS scattering for a steadily heated sample is added in Figure 5 for comparison.

This can be interpreted that thermal denaturation is a process that requires a considerable time span to proceed, as it involves large scale movement of strands. During a picosecond temperature jump, time is too short for the proteins to unfold and the temperature stimulus has vanished before this motion sets in. We deduce a scenario, where a bubble formation process leads to an expulsion of the protein shell from those particles which have surpassed the threshold,[22] while below the threshold hardly any structural modification of the protein shell is induced. The fate of those proteins which are expelled from the particle is not accessible *via* SAXS, but through wide angle scattering that is independent of the SAXS signal from the particles.

Secondary Protein Structure. The SAXS signal contains only information on the radial density distribution around the nanoparticles, and therefore the protein layer can only be modeled by a homogeneous layer. This certainly restricts the amount of information that one can obtain on the protein internal structure such as secondary or further folding motifs. However, at least the secondary motif can directly be addressed by X-ray scattering, keeping in mind that the helix structure is a well-defined longer range order in the protein. In some cases also tertiary or quaternary structure can be resolved for free proteins in solution[23,24] even with high time resolution.[12,25−27] The static wide angle scattering shows indeed a scattering maximum at around 1.35 $Å^{-1}$, which reflects the pitch of the α-helix structure in BSA. Additionally UV circular dichroism data prove that the helical content is unchanged upon the adsorption on gold particles, but reacts on thermal denaturation in a similar way as BSA in solution (static data shown in Figure S3A for the SAXS and Figure S3B for the WAXS part in the Supporting Information).

We have also performed pump−probe scattering with a larger scattering angle, which basically only differs from the SAXS experiment by the distance of the detector from the sample.[14] The main features in these measurements are the change of the water structure factor due to heating and, in particular in the present case, due to expansion of the vapor bubbles and the powder scattering from the crystalline gold particles at Q positions of the (111), (200) and further peaks. Additionally the secondary protein structure gives rise to a scattering distribution at intermediate Q (between the SAXS region, >0.3 $Å^{-1}$, and the liquid scattering peaks, <1.5 $Å^{-1}$), which is subject to changes, if the protein structure is altered. Examples are given in Figure 6, which displays the scattering difference due to laser excitation of different laser fluences at 40, 63, and 140 J/m^2, which relate to temperature rises according to Figure 5 of 80, 120, and 180 K, respectively, in the range where the bubble formation is important for the protein expulsion. A theoretical calculation is performed, using a BSA analogue human serum albumin, entry 1BJ5 in the Protein Data Bank.[28] The atomic coordinates are obtained from this data set and computed into a scattering curve using the program package CRYSOL,[24] which is basically a computation of pairwise atomic scattering contributions by the Debye formula.[29] From this data a structureless SAXS curve has been subtracted, that

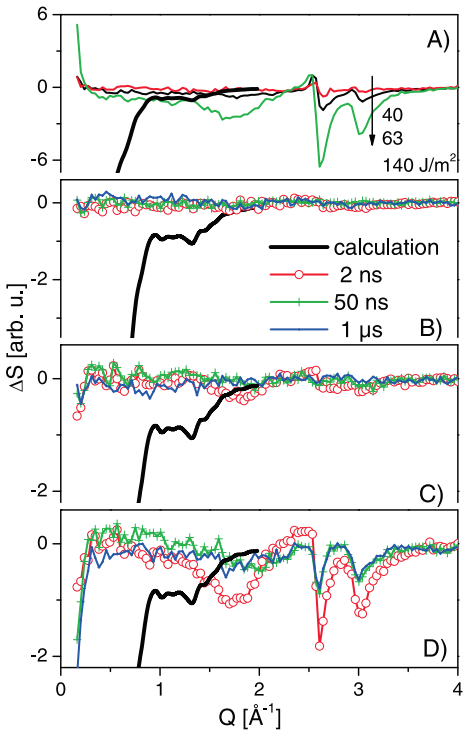

Figure 6. Difference scattering of BSA-coated nanoparticles for various laser fluence values and time delays. (A) The time delay of 350 ps at laser fluences of 40 (red), 63 (black), and 140 J/m^2 (green). (B–D) Data at time delays of 2 ns (red circle), 50 ns (green cross), and 1 μs (blue solid) at laser fluences blow the bubble formation threshold of (B) 40 J/m^2 and (C) 63 J/m^2 and above the threshold of (D) 140 J/m^2. The bold black curve shown up to 2 Å^{-1} in each panel displays the scattering change expected from complete denaturation of a corresponding amount of molecules (see text).

possesses the same radius of gyration and density. By this procedure a transition from a folded protein to a random coil of the same extension is mimicked. The theoretical protein scattering curve can be scaled to absolute units with a standard scaling relation at the high Q limit of the overall water scattering[30,31] and with the use of the amount of adsorbed protein in the suspension. While this model would not properly describe the mesoscale structure in the SAXS region, it would still allow us to monitor the secondary structural motif. This difference structure is overlayed on the time-resolved WAXS curves in Figure 6. One directly can see that in particular of the long time delays of 50 ns and 1 μs the region between 0.9 and 1.5 Å^{-1} does not show any difference signal. This region is governed by the helix peak and does not change with laser fluence (that is whether or not the protein shell is intact or expelled) as would be predicted for the protein denaturation.

For the short time delay at 350 ps and 2 ns only the transient features from the water compression and the Bragg peak changes of the gold particles can be seen. The water structure change would have a minimum around 1.7 and a maximum around 2.3 Å^{-1} [32,30] while the first gold reflections are seen at 2.67 and 3 Å^{-1} as peak shift (positive and negative feature around the nominal powder rings) and as somewhat reduced crystallinity at the high laser fluence for longer delays. In conclusion the wide angle data do not show any changes in the structural motif during transient heating, or during this process of protein expulsion around the bubble formation threshold, which suggests that the expelled proteins are not denaturated in terms of secondary structure. At the highest fluence and 350 ps delay the compressed water signal is, however, higher than the expected protein helix peak, so that one cannot exclude here a short time denaturation during expulsion. The later data from 2 ns is again flat, which do not support this possibility.

CONCLUSION

Gold nanoparticle hybridized with proteins have been photoexcited and analyzed by time-resolved structural techniques, yielding the fastest events in structure formation. Such hybrids are fascinating and yet challenging systems owing to their different levels of complexity both in static structure and photoinduced dynamics. By using pump–probe X-ray scattering, a detailed structural insight in the suspension dynamics and the reaction of the protein shell is achieved. The protein shell can be expelled through the bubble formation process, when surpassing the water spinodal temperature around the heated gold particles. Except for the shell removal no further modifications on the proteins could be observed. It indicates that the protein is relatively unsusceptible to very high, but brief (sub-nanosecond) temperature rise. Longer laser pulses and repetitive excitation on a similar system have been shown to modify the protein structural integrity.[33] The interaction of proteins with inorganic particles acting as local antennae for selective targeting of tissue in biophysical applications is gaining a large amount of interest. Complemented by optical techniques, such as time resolved spectroscopies,[34,35] the presented structural information by ultrafast time-resolved X-ray scattering in the SAXS and WAXS region can provide a valuable contribution to the understanding of dynamics on multiple length scales.

METHODS AND MATERIALS

Pump–Probe Setup. Laser-pump X-ray-probe was performed at the dedicated beamline ID09B at the European Synchrotron Radiation Facility in Grenoble, France. The setup has been described in detail elsewhere.[8,36,37] In brief, an amplified femtosecond laser system (KMLabs) delivers 100 fs pulses of 780 nm

light at a 1 kHz repetition rate. The light is frequency doubled and focused on the liquid jet to about 0.15 mm diameter (full width at half maximum, fwhm). Near-field enhanced ablation from the particles[15,38] was avoided by stretching the laser pulse temporally to about 3 ps by detuning the compressor of the laser amplifier stage. An X-ray mechanical chopper wheel selects X-ray flashes from the storage ring in synchrony to the laser pulses. The 100-ps long X-ray pulses are quasi-monochromatic with a 2.6% bandwidth and a peak wavelength of 0.849 Å[39] and focused onto the liquid jet by a toroidal mirror to about 80 μm fwhm. The scattering is recorded on a CCD (charge coupled device) camera (MarCCD 133) which itself is not time resolving, but records the stroboscopic probe of the structural relaxations as a function of the well-defined time delays between the laser and X-ray pulses. Mutual time delay of the pulses is done with minimal step size of 5 ps by electronic delay units.

The reaction is considered as irreversible, and therefore any portion of the liquid has only been cycled once through the laser-X-ray interaction point and then disposed. The liquid was pumped through an open X-ray capillary at sufficient speed to form a free-flowing liquid jet at the orifice so that interference of the nonflowing particles at the wall with the SAXS signal is avoided. In particular it has been observed that protein-covered particles adsorb on the glass wall (in contrast to bare particles) and are hit multiply by laser pulses, if the capillary is placed in the beam. The scattering from the accumulated debris compromises the scattering distribution considerably. This problem is avoided by using the free jet.

Static SAXS data were collected at the cSAXS beamline[40] at the Swiss Light Source at PSI Villigen (CH) for the determination of the protein adsorption step and the change in shell structure upon thermal denaturation.

X-ray Small Angle and Wide Angle Scattering. Small angle X-ray scattering probes density inhomogeneities in the sample, in the range of nanometers to hundreds of nanometers, depending on the geometry and the instrumental resolution[29,41,42] (see the Supporting Information (SI)). The situation is strongly simplified for scattering objects with spherical symmetry, where for compact gold particles of spherical shape and radius R an analytical function can be given for the form factor:

$$F(Q, R) = 3[\sin(QR) - (QR)\cos(QR)]/(QR)^3 \quad (1)$$

which is a function that shows oscillations at distinct values of the scattering vector Q, which scale with the inverse of the particle size. Core–shell systems can be modeled with a function based on this sphere form factor. A model-independent and useful quantity for the (difference) scattering yield $S(Q)$ is the Porod invariant:

$$P = \int_0^\infty S(Q)Q^2\,dQ = 2\pi^2\Delta\rho^2 {r_e}^2\Phi(1-\Phi) \quad (2)$$

as it allows the derivation of the global scattering length density contrast $\Delta\rho$ change after laser excitation without the need for assumptions on particle shape and size. Φ denotes the filling fraction of the particles total particle volume within the suspension. Φ serves only as a scaling factor for the absolute scattering cross section and is not important here.

The wide angle scattering probes the positional correlation between all atoms in the suspension. This encompasses the structure of the protein molecules, where the most prominent feature to be observed is the helix peak from the helical domains within the protein. Meanwhile the liquid scattering of water dominates the scattering and therefore limits the achievable signal-to-noise ratio in the difference scattering $\Delta S(Q,\tau)$ between the excited system at delay τ and the non-excited system. The bulk water structure responds to changes of temperature and pressure caused by the energy deposition in the absorbing nanoparticles and heat transfer to water. In particular pressure changes caused by expanding vapor bubbles are seen in ΔS.

Importantly all the contributions to the scattering can be modeled quantitatively by using the protein atomic coordinates from the Protein Data Bank and scaling to the water scattering, thus allowing a quantitative prediction of the expected changes due to bubble formation,[20,30] water pressure change,[43] or protein denaturation. Details of the analysis procedure is provided in the Supporting Information

Particle Conjugation. Gold nanoparticles were prepared by the aqueous chemical synthesis method described by Turkevich[44] and optimized for variable size distribution and higher particle density.[45,46] Here we produced particles from a 1.6 mM gold hydrochlorate solution with an average diameter of 15 nm. The size dispersion was around 14%. The batches of gold particle suspension were shipped in polyethylene bottles to the beamline at ESRF and conjugated on site with mercaptosuccinic acid (MCSA, Acros Chemicals, final concentration 0.08 mM) and bovine serum albumin (BSA, Roth, final concentration 3 μM). The MCSA is supposed to act as electrostatic linker between BSA and the gold surface[47] and as spacer. In the Supporting Information more detail on the protein adsorption is given.

Acknowledgment. The research is funded by the Ministry of Science, Education and the Arts Baden-Württemberg and by Creative Research Initiatives (Center for Time-Resolved Diffraction) of MEST/NRF. J.K. and H.I. acknowledge support from the WCU program (R31-2008-000-10071-0). The European Synchrotron Research Facility, Grenoble, and SLS, Villigen, are acknowledged for provision of beamtime and funding. Support by M. Wulff, A. Menzel, and O. Bunk is gratefully acknowledged. A.P. acknowledges the support from the DFG within the Heisenberg fellowship. We would like to thank F. Ciesa, V. Kotaidis, and A. Siems for their help.

Supporting Information Available: Additional information is available on the details of the models used for the description of the SAXS and WAXS signals; the procedure of BSA adsorption on gold nanoparticles; static scattering data from the BSA–nanoparticle hybrids; the circular dichroism measurements on BSA-coated gold particles and the definition of the reaction probability. This material is available free of charge *via* the Internet at http://pubs.acs.org.

REFERENCES AND NOTES

1. Yao, C.; Rahmanzadeh, R.; Endl, E.; Zhang, Z.; Gerdes, J.; Hüttmann, G. Elevation of Plasma Membrane Permeability by Laser Irradiation of Selectively Bound Nanoparticles. *J. Biomed. Opt.* **2005**, *10*, 064012.
2. Yao, C.; Qu, X.; Zhang, Z.; Hüttmann, G.; Rahmanzadeh, R. Influence of Laser Parameters on Nanoparticle-Induced Membrane Permeabilization. *J. Biomed Opt.* **2009**, *14*, 054034.
3. Huang, X.; El-Sayed, I. H.; Qian, W.; El-Sayed, M. A. Cancer Cell Imaging and Photothermal Therapy in the Near-Infrared Region by Using Gold Nanorods. *J. Am. Chem. Soc.* **2006**, *128*, 2115–2010.
4. Hirsch, L. R.; Stafford, R. J.; Bankson, J. A.; Sershen, S. R.; Rivera, B.; Price, R. E.; Hazle, J. D.; Halas, N. J.; West, J. L. Nanoshell-Mediated Near-Infrared Thermal Therapy of Tumors under Magnetic Resonance Guidance. *Proc. Natl. Acad. Sci. U.S.A.* **2003**, *100*, 13549–13554.
5. Pitsillides, C. M.; Joe, E. K.; Wei, X.; Anderson, R. R.; Lin, C. P. Selective Cell Targeting with Light-Absorbing Microparticles and Nanoparticles. *Biophys. J.* **2003**, *84*, 4023–4032.
6. Ihee, H.; Lobastov, V. A.; Gomez, U. M.; Goodson, B. M.; Srinivasan, R.; Ruan, C. Y.; Zewail, A. H. Direct Imaging of Transient Molecular Structures with Ultrafast Diffraction. *Science* **2001**, *291*, 458–461.
7. Lin, M. M.; Shorokhov, D.; Zewail, A. H. Helix-to-Coil Transitions in Proteins: Helicity Resonance in Ultrafast Electron Diffraction. *Chem. Phys. Lett.* **2006**, *420*, 1U7.
8. Plech, A.; Wulff, M.; Bratos, S.; Mirloup, F.; Vuilleumier, R.; Schotte, F.; Anfinrud, P. A. Visualizing Chemical Reactions in Solution by Picosecond X-ray Diffraction. *Phys. Rev. Lett.* **2004**, *92*, 125505.
9. Ihee, H.; Lorenc, M.; Kim, T. K.; Kong, Q. Y.; Cammarata, M.; Lee, J. H.; Bratos, S.; Wulff, M. Ultrafast X-ray Diffraction of Transient Molecular Structures in Solution. *Science* **2005**, *309*, 1223–1227.

10. Ihee, H. Visualizing Solution-Phase Reaction Dynamics with Time-Resolved X-ray Liquidography. *Acc. Chem. Res.* **2009**, *42*, 356–366.
11. Ihee, H.; Wulff, M.; Kim, J.; Adachi, S. Ultrafast X-ray Scattering: Structural Dynamics from Diatomic to Protein Molecules. *Int. Rev. Phys. Chem.* **2010**, *29*, 453–520.
12. Cammarata, M.; Levantino, M.; Schotte, F.; Anfinrud, P. A.; Ewald, F.; Cupane, A.; Wulff, M.; Ihee, H. Tracking the Structural Dynamics of Proteins in Solution Using Time-Resolved Wide-Angle X-ray Scattering. *Nat. Methods* **2008**, *5*, 881–886.
13. Plech, A.; Kotaidis, V.; Grésillon, S.; Dahmen, C.; von Plessen, G. Laser-Induced Heating and Melting of Gold Nanoparticles Studied by Time-Resolved X-ray Scattering. *Phys. Rev. B* **2004**, *70*, 195423.
14. Kotaidis, V.; Dahmen, C.; von Plessen, G.; Springer, F.; Plech, A. Excitation of Nanoscale Vapor Bubbles at the Surface of Gold Nanoparticles in Water. *J. Chem. Phys.* **2006**, *124*, 184702.
15. Plech, A.; Kotaidis, V.; Lorenc, M.; Boneberg, J. Femtosecond Laser Near-Field Ablation from Gold Nanoparticles. *Nat. Phys.* **2006**, *2*, 44–47.
16. Wilson, O. M.; Hu, X.; Cahill, D. G.; Braun, P. V. Colloidal Metal Particles as Probes of Nanoscale Thermal Transport in Fluids. *Phys. Rev. B* **2002**, *66*, 224301.
17. Hu, M.; Hartland, G. Heat Dissipation for Au Particles in Aqueous Solution: Relaxation Time *versus* Size. *J. Phys. Chem. B* **2003**, *107*, 1284–1284.
18. Ge, Z.; Cahill, D. G.; Braun, P. V. Au–Pd Metal Nanoparticles as Probes of Nanoscale Thermal Transport in Aqueous Solution. *J. Phys. Chem. B* **2004**, *108*, 18870–18875.
19. Siems, A.; Weber, S. A. L.; Boneberg, J.; Plech, A. Thermodynamics of Nanosecond Nanobubble Formation at Laser-Excited Metal Nanoparticles. *New. J. Phys.* **2011**, *13*, 043018.
20. Kotaidis, V.; Plech, A. Cavitation Dynamics on the Nanoscale. *Appl. Phys. Lett.* **2005**, *87*, 213102.
21. Jachimska, B.; Wasilewska, M.; Adamczyk, Z. Characterization of Globular Protein Solutions by Dynamic Light Scattering, Electrophoretic Mobility, and Viscosity Measurements. *Langmuir* **2008**, *24*, 6866–6872.
22. Jain, P. K.; Qian, W.; El-Sayed, M. A. Ultrafast Cooling of Photoexcited Electrons in Gold Nanoparticle–Thiolated DNA Conjugates Involves the Dissociation of the Gold–Thiol Bond. *J. Am. Chem. Soc.* **2006**, *128*, 2426–2433.
23. Svergun, D. I.; Petoukhov, M. V.; Koch, M. H. Determination of Domain Structure of Proteins from X-ray Solution Scattering. *Biophys. J.* **2001**, *80*, 2946–2953.
24. Svergun, D. I.; Koch, M. H. Advances in Structure Analysis Using Small-Angle Scattering in Solution. *Curr. Opin. Struct. Biol.* **2002**, *12*, 654–660.
25. Ahn, S.; Kim, K. H.; Kim, Y.; Kim, J.; Ihee, H. Protein Tertiary Structural Changes Visualized by Time-Resolved X-ray Solution Scattering. *J. Phys. Chem. B* **2009**, *113*, 13131–13133.
26. Kim, J.; Kim, K. H.; Kim, J. G.; Kim, T. W.; Kim, Y.; Ihee, H. Anisotropic Picosecond X-ray Solution Scattering from Photoselectively Aligned Protein Molecules. *J. Phys. Chem. Lett.* **2011**, *2*, 350–356.
27. Kim, K. H.; Oang, K. Y.; Kim, J.; Lee, J. H.; Kim, Y.; Ihee, H. Direct Observation of Myoglobin Structural Dynamics from 100 Picoseconds to 1 Microsecond with Picosecond X-ray Solution Scattering. *Chem. Commun.* **2011**, *47*, 289–291.
28. Curry, S.; Mandelkow, H.; Brick, P.; Franks, N. Crystal Structure of Human Serum Albumin Complexed with Fatty Acid Reveals an Asymmetric Distribution of Binding Sites. *Nat. Struct. Biol.* **1998**, *5*, 827–835; PDB entry 1BJ5.
29. Warren, B. E. *X-ray Diffraction* (reprint); Dover Publications: New York, 1990.
30. Plech, A.; Kotaidis, V.; Lorenc, M.; Wulff, M. Thermal Dynamics in Laser Excited Metal Nanoparticles. *Chem. Phys. Lett.* **2005**, *401*, 565–569.
31. Kim, T.-K.; Lorenc, M.; Lee, J.-H.; Russo, M. L.; Kim, J.; Cammarata, M.; Kong, Q.; Noël, S.; Plech, A.; Wulff, M.; *et al.* Spatiotemporal Reaction Kinetics of an Ultrafast Photoreaction Pathway Visualized by Time-Resolved Liquid X-ray Diffraction. *Proc. Natl. Acad. Sci. U.S.A.* **2006**, *103*, 9410–9415.
32. Haldrup, K.; Christensen, M.; Nielsen, M. M. Analysis of Time-Resolved X-Ray Scattering Data from Solution-State Systems. *Acta Cryst.* **2010**, *A66*, 261–269.
33. Takeda, Y.; Mafuné, F.; Kondow, T. Selective Degradation of Proteins by Laser Irradiation onto Gold Nanoparticles in Solution. *J. Phys. Chem. C* **2009**, *113*, 5027–5030.
34. Bredenbeck, J.; Helbing, J.; Sieg, A.; Schrader, T.; Zinth, W.; Renner, C.; Behrendt, R.; Moroder, L.; Wachtveitl, J.; Hamm, P. Picosecond Conformational Transition and Equilibration of a Cyclic Peptide. *Proc. Natl. Acad. Sci. U.S.A.* **2003**, *100*, 6452–6457.
35. Dartigalongue, T.; Hache, F. Calculation of the Circular Dichroism Spectra of Carbon Monoxy- and Deoxy-myoglobin: Interpretation of a Time-Resolved Circular Dichroism Experiment. *J. Chem. Phys.* **2005**, *123*, 184901.
36. Wulff, M.; Schotte, F.; Naylor, G.; Bourgeois, D.; Moffat, K.; Mourou, G. Time-Resolved Structures of Macromolecules at the ESRF: Single-Pulse Laue Diffraction, Stroboscopic Data Collection and Femtosecond Flash Photolysis. *Nucl. Instr. Meth. Phys. Res. A* **1997**, *398*, 69–84.
37. Cammarata, M.; Eybert, L.; Ewald, F.; Reichenbach, W.; Wulff, M.; Anfinrud, P.; Schotte, F.; Plech, A.; Kong, Q.; Lorenc, M.; *et al*. Optimized Shutter Train Operation for High Brightness Synchrotron Pump–Probe Experiment. *Rev. Sci. Instr.* **2009**, *80*, 015101.
38. Plech, A.; Boneberg, J.; Leiderer, P. Femtosecond Laser Near-Field Ablation. *Laser Photonics Rev.* **2009**, *3*, 435–451.
39. Plech, A.; Randler, R.; Geis, A.; Wulff, M. Diffuse Scattering from Liquid Solutions with White Beam Undulator Radiation for Photoexcitation Studies. *J. Synchrotron Radiat.* **2002**, *9*, 287–292.
40. Henkel, A.; Schubert, O.; Plech, A.; Sönnichsen, C. Growth Kinetic of a Rod-Shaped Metal Nanocrystal. *J. Phys. Chem. C* **2009**, *113*, 10390–10394.
41. Guinier, A.; Fournet, G. *Small-Angle Scattering of X-Rays*; John Wiley & Sons: New York, 1955.
42. Dingenouts, N.; Bolze, J.; Pötschke, D.; Ballauff, M. Analysis of Polymer Latexes by Small-Angle X-Ray Scattering. *Adv. Polym. Sci.* **1999**, *144*, 1–47.
43. Cammarata, M.; Lorenc, M.; Kim, T. K.; Lee, J. H.; Kong, Q. Y.; Pontecorvo, E.; Russo, M. L.; Schiró, G.; Cupane, A.; Wulff, M.; *et al*. Impulsive Solvent Heating Probed by Picosecond X-ray Diffraction. *J. Chem. Phys.* **2006**, *124*, 124504.
44. Turkevich, J.; Stevenson, P. C.; Hillier, J. A Study of the Nucleation and Growth Processes in the Synthesis of Colloidal Gold. *Discuss. Faraday Soc.* **1951**, *11*, 55–75.
45. Kimling, J.; Maier, M.; Okenve, B.; Kotaidis, V.; Ballot, H.; Plech, A. Turkevich Method for Gold Nanoparticle Synthesis Revisited. *J. Phys. Chem. B* **2006**, *110*, 15700–15707.
46. Frens, G. Controlled Nucleation for the Regulation of the Particle Size in Monodisperse Gold Suspensions. *Nat. Phys. Sci.* **1973**, *241*, 20–22.
47. Kaufman, E. D.; Belyea, J.; Johnson, M. C.; Nicholson, Z. M.; Ricks, J. L.; Shah, P. K.; Bayless, M.; Pettersson, T.; Feldoto, Z.; Blomberg, E.; *et al*. Probing Protein Adsorption onto Mercaptoundecanoic Acid Stabilized Gold Nanoparticles and Surfaces by Quartz Crystal Microbalance and ζ-Potential Measurements. *Langmuir* **2007**, *23*, 6053–6062.